Applied Surface Science 456 (2018) 360–368

Contents lists available at ScienceDirect

Applied Surface Science

journal homepage: www.elsevier.com/locate/apsusc

Full Length Article

Morphology controlled synthesis of $CeTiO_4$ using molten salts and enhanced photocatalytic activity for CO_2 reduction

Reshalaiti Hailili[a,b], Daniel L. Jacobs[c], Ling Zang[c,*], Chuanyi Wang[a,b,*]

[a] Laboratory of Environmental Sciences and Technology, Xinjiang Technical Institute of Physics & Chemistry, Key Laboratory of Functional Materials and Devices for Special Environments, Chinese Academy of Sciences, Urumqi 830011, China
[b] School of Environmental Science and Engineering, Shaanxi University of Science and Technology, Xi'an 710021, China
[c] Nano Institute of Utah and Department of Materials Science and Engineering, University of Utah, Salt Lake City, UT 84112, USA

ARTICLE INFO

Keywords:
$CeTiO_4$
Molten salt synthesis
Visible light
CO_2 Photoreduction

ABSTRACT

Incorporation of visible light active semiconductors without doping noble (transition) metals results in remarkably different construction principle of visible light driven photocatalysts in which light absorptions and charge transfer become more flexible and efficiencies are no longer limited in ultraviolet (UV) region. Herein, we provide a strategy to design efficient photocatalysts by introducing visible light sensitive Ce_2O_3 into UV active TiO_2 via molten salt synthesis (MSS) of $CeTiO_4$ for visible light CO_2 reduction. By changing salt composition in the MSS process, the nanostructured $CeTiO_4$ was prepared and exhibited distinct morphologies e.g., nanorods ($NaCl-NaH_2PO_4$), polyhedrons ($KCl-NaCl$) and cubic ($KCl-Na_2SO_4$), respectively. Of the different morphologies, the nanorods of $CeTiO_4$ showed best photoactiviy with quantum efficiencies of 0.36% and 0.065% for CO and CH_4 formation, respectively. The unique morphologies well positioned band edges cause such obvious differences and co-contribute to the high performance effectiveness. This study demonstrates a strategy for the rational design and fabrication of visible light driven photocatalysts with controlled morphology, which in turn, can enhance the control and production of value-added products of CO_2 reduction. This is an important step towards realizing the utilization of renewable energy sources, such as solar power, to reduce the concentration of atmospheric CO_2 and form green energy sources.

1. Introduction

The increase of industrialization driven by fossil fuel energies is causing increasing amounts of atmospheric CO_2. This increase in CO_2, an important greenhouse gas, is a leading source of the increase in global temperatures, which contributes toward to growing societal problems throughout the world [1]. One important strategy to mitigate future risk of rising CO_2 concentrations is CO_2 capture and conversion to value-added compounds such as CO, CH_4 and CH_3OH [2,3]. Semiconductor based photocatalytic technique to convert CO_2 is a very promising approach pioneered with the first milestone work of photoelectrochemical reduction reported by Halmann in 1978 and photocatalytic CO_2 reduction by Inoue in 1979 [4,5]. Photocatalysis, moreover, has the advantage that the driving force is the inexhaustible and endless supply of sun light. Numerous semiconductors have been explored for photocatalytic approach, for instance TiO_2, Zn_2GeO_4, CdS, $ZnGa_2O_4$, MOF (metal-organic framework) and so on [6–13]. TiO_2 in particular, has exhibited exceptional photocatalytic performance, leading to the TiO_2-based catalysts with further improved properties [14–20]. However, widely studied semiconductors are only active under ultraviolet (UV) light and the majority of them suffer from low quantum yields and instability because of relatively large electronic band gap and quick recombination of photoinduced electron–hole pairs [1–3]. Therefore, the main challenge is searching for potential photocatalysts, which are stable, environmental friendly, have a suitable band gap and can effectively separate charge carriers, subsequently accelerate visible light conversion of CO_2 to useful fuels at a reasonable rate.

One method to improve the light absorption of high efficiency photocatalysts, such as TiO_2, is to incorporate visible light active materials, e.g., noble metals [14]. However, noble metals can be rare and expensive and therefore would be hard to scale. Incorporation of transition metals is another approach to improving the visible light efficiency. In particular, cerium has been shown to display promising co-catalytic properties in CO_2 reduction systems, is nontoxic, and is very abundant in the earth's crust (66.5 ppm), greater even than copper

* Corresponding authors at: Laboratory of Environmental Sciences and Technology, Xinjiang Technical Institute of Physics & Chemistry, Key Laboratory of Functional Materials and Devices for Special Environments, Chinese Academy of Sciences, Urumqi 830011, China (C. Wang).
E-mail addresses: lzang@eng.utah.edu (L. Zang), wangchuanyi@sust.edu.cn (C. Wang).

https://doi.org/10.1016/j.apsusc.2018.06.048
Received 22 March 2018; Received in revised form 4 June 2018; Accepted 7 June 2018
Available online 15 June 2018
0169-4332/ © 2018 Elsevier B.V. All rights reserved.

(60 ppm) [21]. More significantly, Ce_2O_3 is a visible light sensitive semiconductor with a band gap of 2.40 eV [22]. In the view of efficient utilization of solar energy, Ce—Ti—O system are widely studied, among which $CeTiO_4$ is considered as a promising alternative visible light active photocatalyst compared to noble metal catalyst systems [23–26].

Beyond improving the light absorption, one of the most important factors of photocatalytic reduction of CO_2 is efficient adsorption of CO_2 on the surface of catalysts [27,28]. The redox potential of the photo-induced electron–hole pairs and the surface charge distribution is dependent on the catalyst's surface, where occurs the chemical redox reaction, adsorption of the reactant to reduce the detrimental problem of fast charge carrier recombination and enhance photoreduction [29]. Moreover, the activity of photocatalysts not only depends on the intrinsic physical properties but it relates to the material's crystalline size, morphology, defects as well as other surface properties [30,31]. These extrinsic properties can be tuned by changing preparation methods and reaction conditions. Molten salt synthesis (MSS) is an effective approach to control morphology due to its advantages in facilitating crystal growth with improved phase-purity based on varying the salt compositions, molar ratio and reaction temperature [29–31]. However, compared to simple metal oxides, control of crystalline growth of complex oxide photocatalysts is proven more difficult due to the complex bonding relations and atomic charge balance interactions in the crystal lattice. Therefore, morphology tailoring of complex oxides is greatly needed to further improve their photocatalytic performance in practical applications.

Motivated by the above discussions, we present one-step, facile synthesis of a visible light active catalyst $CeTiO_4$ as an efficient photocatalyst for CO_2 reduction. Morphology tailoring was achieved with a MSS by changing the salt compositions, which gave short nanorods, polyhedron and cube shapes. As-obtained samples exhibited both a reduction in the band gap, compared to TiO_2, as well as shifting of the conduction and valence band energy levels to enhance CO_2 reduction under visible light irradiation. The products of CO_2 reduction in the presence of $CeTiO_4$ samples showed more favourable for CO formation over CH_4. Among obtained samples, the short nanorods of $CeTiO_4$ exhibited the highest efficiency with nearly 0.355% and 0.065% quantum efficiencies for CO and CH_4 formation, respectively. This is about 12 and 32 times higher than that of reported TiO_2 anatase-rutile (0.029%) and Fe, S doped $Sr_3Ti_2O_7$ (0.011%) for preferred CO formation under visible light irradiation [32,33]. The diverse morphologies, well crystallinity and suitable thermodynamics were co-contributing for the improved photocatalytic activity. To the best of our knowledge, this is the first example of controlled synthesis of $CeTiO_4$ with distinct morphology and visible light driven photocatalytic property towards CO_2 reduction.

2. Experimental section

2.1. Preparation of samples

All chemical reagents used in this experiment were of analytic grade and used without further purification. $CeTiO_4$ catalyst was prepared by molten salt method in various salt systems. The typical synthetic procedures of sample **1**–sample **3** are identical, except for the salt composition, which are listed in Table 1. The stoichiometric mixture of the analytic reagent grade raw materials $Ce(NO_3)_3{\cdot}6H_2O$ (as a Ce_2O_3 source) and TiO_2 were added to the different salts system with a mole ratio of $CeTiO_4$:M_{S1}:M_{S2} = 1:8:8 (M_{S1}, M_{S2} is mole ratio of employed salts). The mixtures were ball-milled in a small amount of ethanol for 3 h. Then, the dried mixture was heated in the corundum crucible at 200 °C for 2 h, subsequently increased to 600 °C and dweller for 10 h, cooled to 300 °C for 2 h, further slowly cooled to 200 °C at a rate of 1 °C/min and kept for 2 h, and finally cooled to room temperature at a rate of 1 °C/min. As-obtained samples were washed with water for two days to remove the salts, dried at 60 °C for 12 h for characterization or photocatalytic testing.

2.2. General remarks

The crystal structure of the $CeTiO_4$ samples was studied using a Bruker AXS D8 diffractometer operating at 40 kV with a scan step width of 0.02° and a fixed counting time of 1 s/step using an graphite monochromator set for Cu Kα (λ = 1.5418 Å) radiation in the angular of 2 θ from 10° to 70°. The relative metal amounts were determined by inductively coupled plasma optical emission spectrometry (ICP, VISTA-PRO). Before the ICP measurements, the samples were hydrothermally treated with HNO_3 at 180 °C for 3 h. The morphology of samples was analyzed with field-emission scanning electron microscopy (FESEM, ZEISS SUPRA55VP). Transmission electron microscopy (TEM) characterizations of as-obtained samples were performed on a JEOL–JEM 2100 electron microscope. Optical absorption was analyzed based on diffuse reflectance spectra on 40.0 mg of as-obtained products at room temperature using in ultraviolet-visible region taken on a spectrometer (Solid Spec-3700DUV Shimadzu) equipped with an integrating sphere. The $BaSO_4$ was used as a reference material to base line correction within the wavelength range 200 nm–800 nm. The electron paramagnetic resonance (EPR) spectrum of per 20.0 mg samples was characterized with Bruker E500 Spectrophotometer. The specific BET surface area of per 30.0 mg samples was determined with Brunauer–Emmett–Teller (BET) method from nitrogen adsorption–desorption isotherms recorded at 77 K on a Quantachrome instrument (QUADRASORB IQ). The samples were outgassed at 180 °C for 3 h before the measurements.

2.3. Photocurrent response measurements

Photocurrent measurements were conducted on an electrochemical workstation with a standard three-electrode system in 0.1 mol·L^{-1} of Na_2SO_4 electrolyte solution. The prepared sample electrode (per 5.0 mg of samples were dispersed in an ITO glass substrate with an area ~1.0 cm^2), saturated calomel electrode and platinum electrode were used as the working electrode, reference electrode and counter electrode, respectively. The intensity of photocurrent were measured by an electrochemical workstation (CHI660, Chenhua Instrument, Shanghai, China) and the 300 W Xe lamp was used as light source.

2.4. Photoreduction experiments

The photocatalytic reduction of CO_2 with H_2O vapor was carried out in a reactor connected with mechanical vacuum pump with a gas-closed circulating system. Gaseous CO_2 was produced on site in a reactor by the reaction of $NaHCO_3$ (analytical grade) with 0.5 mol·L^{-1} H_2SO_4 solution, providing a mixture of CO_2 and H_2O vapor. The photocatalyst

Table 1
The reaction conditions, ICP analyses and morphologies of sample **1**–sample **3.**

Sample no.	Salt composition	Ce:Ti	Morphology	Length (nm)	Diameter (nm)
Sample **1**	NaCI—NaH_2PO_4	0.93:0.92	Short nanorod	200–400	30–80
Sample **2**	KCI—NaCI	0.89:0.95	Polyhedron	50–100	40–60
Sample **3**	KCI—Na_2SO_4	0.94:0.88	Nanocube	50–100	5–10

powder (20.0 mg) was evenly deposited on a circular quartz plate and then placed inside the photo-reactor perpendicular to the light beam, which was operated in an air-tight container under atmospheric pressure at ambient temperature. After that, the reaction system was vacuum treated to form an air-free system and maintained for 60 min for CO_2 adsorption, then irradiated with a 300 W Xe lamp (PLS-SXE300, Perfect Light Company, Beijing, China) equipped with a UV cutoff filter (420 nm) as light source. The photocatalytic experiment of CO_2 reduction with H_2O was carried out at 298 K for 7 h in each run. The products of CO and CH_4 were continuously analyzed for different times (h) in situ by online gas chromatography (GC, Agilent 7890A) with a TCD detector equipped with Molsieve 5 Å column using H_2 as carrier gas.

3. Results and discussion

3.1. Synthesis and characterization of photocatalysts

During the process of molten salt synthesis (MSS), specific salt compositions have a significant effect on the morphology and characteristics of resulted photocatalysts. Thus, MSS was utilized to tune the material properties of $CeTiO_4$ photocatalyst by changing salt compositions during crystal growth process. Compared with common salts, utilizing eutectic salt compositions enables a lower reaction temperature and enhances the ion mobility [34]. For instance, the melting point (m.p.) of pure salts NaCl and KCl is about 801 °C and 776 °C, respectively, while NaCl−KCl eutectic composition acquires a relatively lowered m.p. = 645 °C. Therefore, we select mixture of common salts in order to reduce the calcinations temperature and increase the ion mobility. The different salt compositions used in the MSS process for synthesis of $CeTiO_4$ were NaCl−NaH_2PO_4 (sample **1**), KCl−NaCl (sample **2**) and KCl−Na_2SO_4 (sample **3**).

Fig. 1 shows the corresponding XRD patterns of the synthesized sample **1**–sample **3** and used TiO_2. Without any salts, the obtained diffraction patterns are corresponding to the characteristic peaks of a $Ce_{2/3}TiO_3$ phase [23,24]. When molten salts were introduced into the system, the intensities of characteristic diffraction peaks at around 22.7–22.8° from $Ce_{2/3}TiO_3$ diminished, followed by appearance of peaks distinct from the sample prepared without molten salt as depicted in Fig. 1.

The obtained diffraction peaks were determined to be characteristic peaks of $CeTiO_4$ based on comparison with the reported literature [24]. Previously reported $CeTiO_4$ was obtained by combining two parent metal oxides (CeO_2 and TiO_2) at very high temperature of 1500 °C and undergo further heating at 450–500 °C [25]. Herein by employing molten salt and programmed control of reaction temperature, we obtained pure phase of $CeTiO_4$, which was matched well with phase of $CeTiO_4$ [24]. We assume that its successful synthesis could be attributed to the effective oxidization of $Ce_{2/3}TiO_3$ and stepwise ionization of introduced salts. With mild preparation conditions of MSS, the phase alteration of $Ce_{2/3}TiO_3$ take place to generate $CeTiO_4$ instead of formation of combined oxide CeO_2−TiO_2 as it is surrounded by Ce ions, enhanced formation of Ti−O−Ce bonds. Moreover, the relatively smaller ionic radius of Ti^{4+} (0.068 pm) would substitute in the structure of Ce_2O_3 (Ce^{3+} = 0.094 pm) and hamper its crystallization into cubic phase because of sufficient and increased Ti amounts in the structure [22,35].

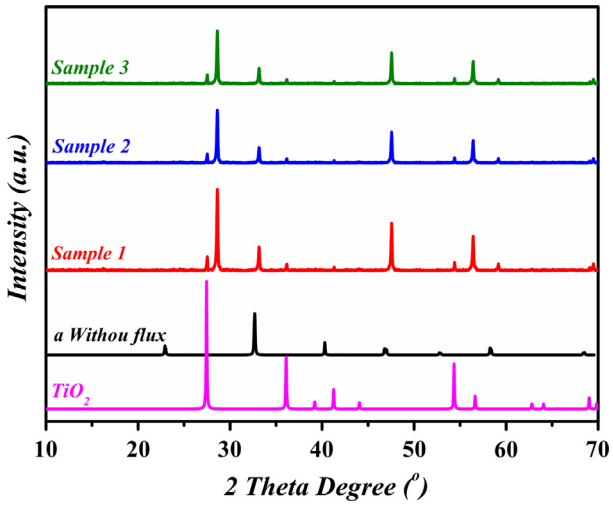

Fig. 1. XRD patterns of as-obtained sample **1**–sample **3** and TiO_2.

The ICP analysis was further applied for the accurate compositions of samples. As listed in Table 1, relative ratio of Ce and Ti in the samples was determined to be ~0.9:0.9, almost close to the composition ratio of Ce:Ti = 1:1, indicating that as-prepared samples could be confirmed as the pure phase of $CeTiO_4$.

Morphologies of as-obtained $CeTiO_4$ catalysts were observed by scanning electron microscopy (SEM) as exhibited in Figs. 2 and 3, in which microstructures of $CeTiO_4$ vary drastically across diverse salt compositions introduced in the MSS process. The NaCl−NaH_2PO_4 salt system used in sample **1** results in short nanorod with an average length and diameter in the range of 200 nm–400 nm and 30 nm–80 nm, respectively, the product yields of as-observed short nanorods about 95%. To further verify the microstructures of sample **1**, the detailed morphologies were observed by TEM analysis. As shown in Fig. 2b, the sample **1** exhibits short nanorods morphology with the average length of about 200 nm–350 nm and the diameter is about 40 nm–60 nm, which are consistent with observed SEM images (Fig. 2a). On the basis of observed crystal structure and SEM images, we assume there is predominant exposed facets in sample **1**. However, the lack of a fully defined crystal unit structure of $CeTiO_4$ limits the ability to identify inter-planar confirmation, thus, the corresponding exposed facets and orientated growth orientation of sample **1** cannot be determined herein.

With KCl−NaCl, the observed morphology of sample **2** exhibits a polyhedron-shaped $CeTiO_4$ (the product yield of 98%) with an average length in the range of 50 nm–100 nm and diameter of 40 nm–60 nm (Fig. 3a). Such a uniform morphology and high product yields may ascribe to the relatively low melting point of selected salt KCl−NaCl (645 °C). The TEM images of sample **2** are shown in Fig. 3b and exhibit polyhedrons, which is quite consistent with obtained SEM observations (Fig. 3a). As-obtained polyhedron in sample **2** was not uniform, implying existence of defects in the structure (Fig. 3b). This observed defects may be ascribed to the unique synthetic approach since the molten salt reaction follows a ionization-nucleation-crystallization-recrystallization process [29]. Finally, by using KCl−Na_2SO_4 salt system, sample **3** displays a uniform cube shaped morphology (Fig. 3c). Close examination of these nanocubes reveals that a large portion of the cubes have critical dimensions around 50 nm, high uniformity and product yields of about 95%. The crystallinity of obtained nanocubes (sample **3**) was further investigated by TEM analysis (Fig. 3d). A single nanocube taken from sample **3** is shown in the inset image in Fig. 3d highlights the high level of crystallinity and uniformity of the nanocubes. Synthesis of highly uniformed short nanocubes within 100 nm of length, like sample **3**, proved to be intriguing yet challenging in conventional preparation methods. When the molten salts are employed into the synthesis, the nucleation and growth rates will effect and the step by step ionization of introduced salts contribute to the diverse and highly uniform morphologies evidenced in sample **1**–sample **3**. As such, the formation of nanosized catalysts is mainly ascribed to the selected molten salt. It's worth mentioning that these obtained Ce, Ti-based compounds with nanocubes structure have a sizes of about 50 nm, which has never been reported up to date to the best of our knowledge.

Above SEM and TEM results show that distinct morphological $CeTiO_4$ are obtained in the MSS, and such dramatic morphology differentiations may originate from the crucial roles of variation of the salt

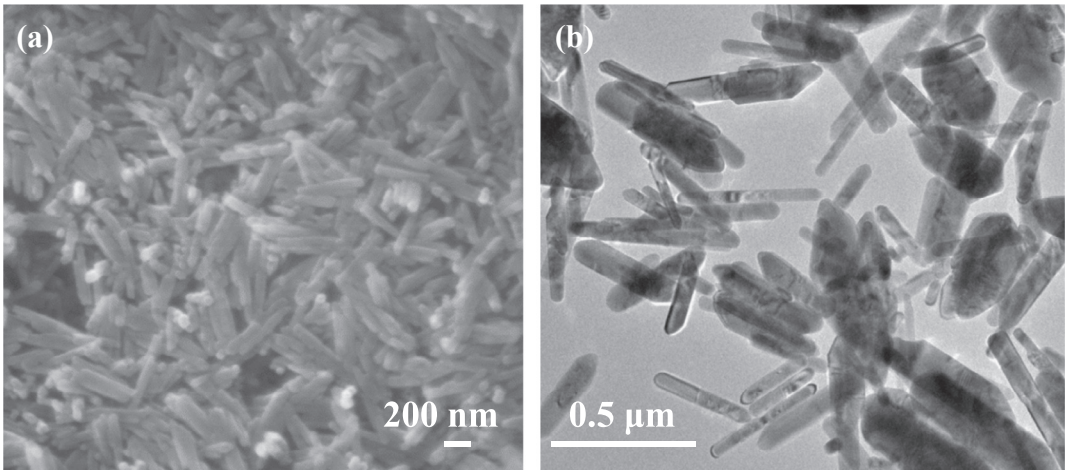

Fig. 2. SEM and TEM images of short nanorods of sample **1** fabricated in NaCl—NaH_2PO_4.

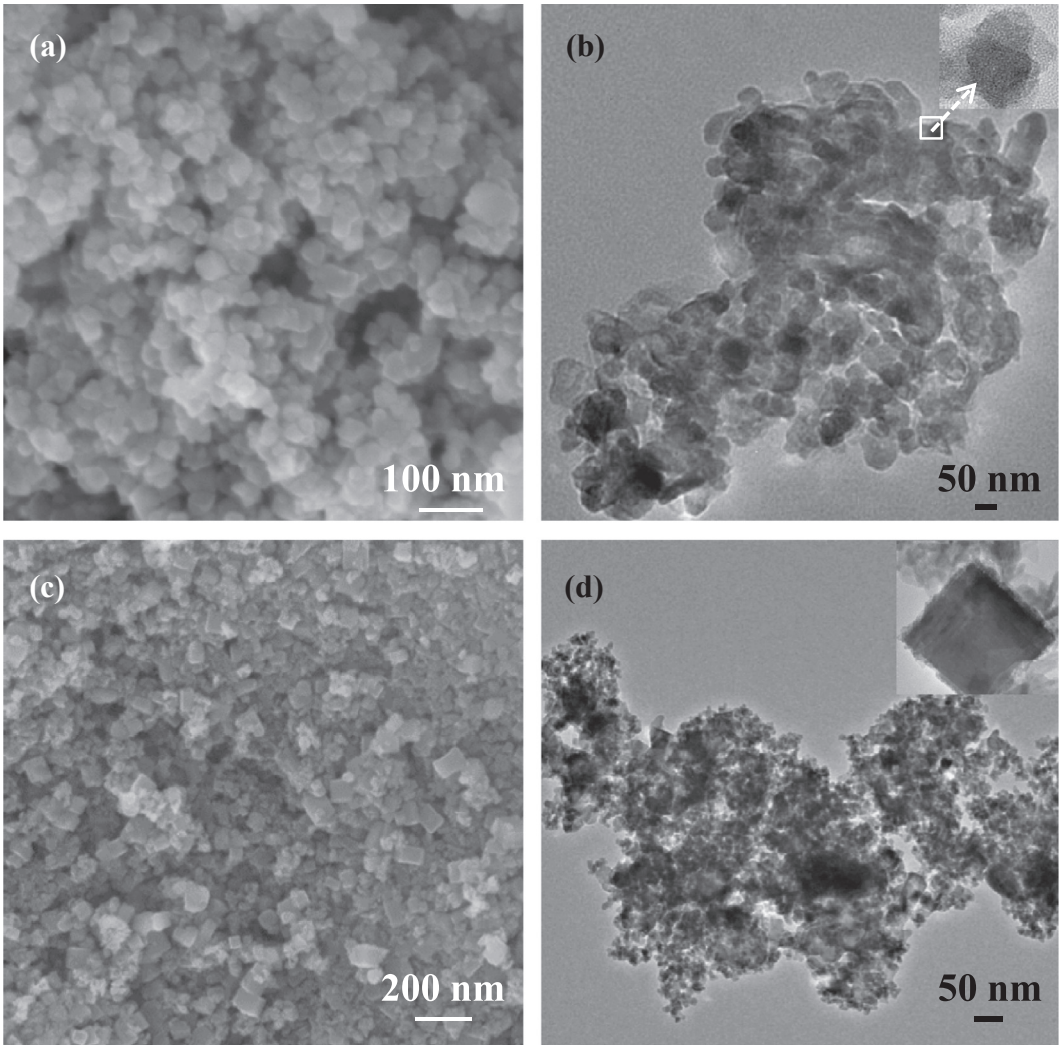

Fig. 3. (a) Uniform polyhedrons obtained in sample **2** with the assistance of KCl—NaCl molten salt; (b) TEM image of polyhedrons and HRTEM image recorded at the marked area of polyhedron in sample **2**; (c) SEM images of nanocube shaped sample **3** obtained in the molten salt KCl—Na_2SO_4; (d) TEM image of individual nanocubes and corresponding image recorded at the selected area of panel.

composition. Meanwhile the highly uniform morphologies further confirms their phase purities. First step of MSS is salt ionization as the temperature increasing to its molten point to form cations and ions, which are mainly play vital roles and responsible for various morphologies. Thus, flux agent selection is one of significantly vital factors, which can directly influences the microstructures of samples. For example, in sample **1**, the chlorides (Cl^-) and phosphate ions ($H_2PO_4^-$) formed from the introduced molten salt (NaCI—NaH_2PO_4)

and are absorbed on the sites of sample, which acquires relatively higher surface energy of the crystals (edges, corners or specific index surface) and leading to decrease the surface energy [29]. This is considered to be the primarily reason for unusual stability and different morphology of sample **1** during the crystallization process. Besides, during the reaction, the phosphate ions ($H_2PO_4^-$) as a mineralizing agent play a major role in forming short nanorods with uniform smooth surface in sample **1**. Same observations of octahedron shaped CeO_2 morphology was obtained with the assistance of $H_2PO_4^-$ as a mineralized agent [36]. As the case of sample **2**–sample **3**, the obtained morphologies are polyhedron and nanocube shaped crystals, which are ascribed to be the main role of anions (Cl^- and SO_4^{2-}) in the syntheses. However, the main reasons for formation of different morphology of nanostructures assembled in molten salts are still controversial, to clarify this, factors such as salt solubility, the thermodynamics and kinetic may considered. The specific morphologies and corresponding element compositions of sample **1**–sample **3** are summarized in Table 1.

3.2. Evaluation of photocatalytic activity

The photocatalytic activity evaluations were examined via photoreduction of CO_2 in the presence of H_2O vapor under visible light irradiation. Both carbon monoxide (CO) and methane (CH_4) were produced as the main products of CO_2 photoreduction over the as-prepared samples. To understand the photoreduction process and activity of the samples, a series of blank experiments were carried out and show that neither CH_4 nor CO generated without light, catalyst, or CO_2, which confirms the photocatalytic ability of the $CeTiO_4$ samples. Fig. 4a shows

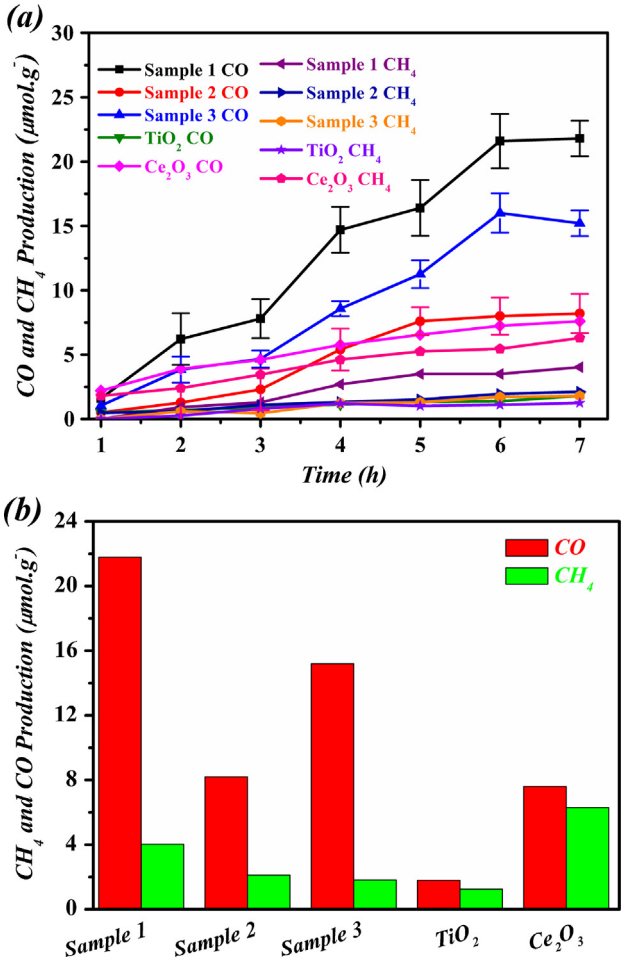

Fig. 4. CH_4 and CO evolutions in the presece of sample **1**–sample **3** and references Ce_2O_3 and TiO_2.

the overall CO and CH_4 production over time from sample **1**–sample **3** under continuous visible light irradiation. The samples show a steady increase in the CO and CH_4 production over time up to 7 h. Comparative tests of visible light CO_2 reduction over reference materials (TiO_2 and Ce_2O_3) were also conducted, respectively. Results show that both parent oxides are tend to produce CO more than CH_4, in which relatively higher efficiencies are observed in Ce_2O_3. After 7 h irradiation of visible light, the generation rates of CH_4 were calculated to be 0.58 μmol·g^{-1}·h^{-1} (sample **1**), 0.31 μmol·g^{-1}·h^{-1} (sample **2**) and 0.26 μmol·g^{-1}·h^{-1} (sample **3**), respectively. Alternatively, the production rates of CO were determined to be 3.11 μmol·g^{-1}·h^{-1}, 1.18 μmol·g^{-1}·h^{-1} and 2.18 μmol·g^{-1}·h^{-1} over sample **1**–sample **3**, respectively. It can be seen from these results that all as-obtained $CeTiO_4$ samples show higher reduction efficiencies to CO compared to CH_4. For both CO and CH_4 production, sample **1** showed the highest generation rates, in that order. The same observations of CO production preference over CH_4 were reported on $NaCeTi_2O_6$ and 3DOM TiO_2-supported CeO_2 [37,38]. Besides, Ce_2O_3 is tend to produce more CH_4 than all studied samples with a generation rate of 0.9 μmol·g^{-1}·h^{-1}, while TiO_2 merely shows 0.17 μmol·g^{-1}·h^{-1} formation. Interestingly, it can be seen from reduction results that as-obtained $CeTiO_4$ samples produce even much more CO than both parent oxides Ce_2O_3 and TiO_2. For instance, the CO generation rate over sample **1** is about 12.44 and 2.87 times larger than CO generation in the presence of TiO_2 and Ce_2O_3, respectively. These results are shown in Fig. 4 and summarized in Table 2.

To evaluate the energy conversion efficiency of samples, the quantum efficiency (QE) of CO_2 was calculated according to the following equations [39]:

$$QE = \left(\frac{n_1 M(CH_4) N_A h\nu}{I_0 \lambda S t}\right) \quad \text{and} \quad QE = \left(\frac{n_2 M(CO) N_A h\nu}{I_0 \lambda S t}\right)$$

where *QE* is the quantum efficiency, *n* is the required electron number (n_1 = 8 for CH_4, n_2 = 2 for CO) for formation products; *M* (CH_4) and *M* (CO) is the yield of CH_4 and CO; N_A is the Avogadro constant; *h* is Planck's constant; *ν* is the speed of light under vacuum; λ is the wavelength; I_o is the total optical intensity of light; *S* is the area of illumination, and *t* is the irradiation time, respectively. The QE of generated CO over sample **1**–sample **3** are 0.355% (sample **1**) > 0.249% (sample **3**) > 0.135% (sample **2**), respectively. Correspondingly, the calculated QE for CH_4 evolution over studied samples are 0.065% (sample **1**) > 0.035% (sample **2**) > 0.029% (sample **3**), respectively. Obviously, with short nanorod morphology, sample **1** displays relatively higher photocatalytic efficiency with approximately 0.355% and 0.065% QEs for CO and CH_4 production, respectively. This result is nearly 12, 2.6 and 32 times higher than that of reported visible light active photocatalysts, defective TiO_2 anatase-rutile (0.029%), {0 0 1}-{1 0 1} coexposed faceted TiO_{2-x} (0.134%) and Fe, S doped $Sr_3Ti_2O_7$ (0.011%) for CO formation under visible light irradiation [19,32,33]. The corresponding QE (%) of other samples are listed in Table 2.

3.3. Clarification of the CO_2 photoreduction mechanism

In photocatalytic systems, light with energy larger or equal to band gap of a semiconductor is necessary to excite electrons from valence band to conduction band, leaving equal numbers of holes in the valence band. The photogenerated electrons in the CB can recombine rapidly with holes in the VB, though in the presence of redox reactive components, the photogenerated electron–hole pairs induce photoreduction and photooxidation reactions. At the conduction band, the excited electrons transfer to the surface of a photocatalyst and react with CO_2 to reduce it to form solar fuels such as CO or CH_4 as described by the following reactions:

$CO_2 + 2\ e^- + 2H^+ \rightarrow CO + H_2O$ ($E^\circ_{red} = -0.53$ V vs. NHE, pH = 7.00)

Table 2
The detailed morphologies, optical properties, BET results, generation rates and corresponding quantum efficiencies of CO_2 reduction products over sample **1**–sample **3**.

Sample no.	Morphology	Band gap (eV)	BET ($m^2 \cdot g^{-1}$)	Generation rate ($\mu mol \cdot g^{-1} \cdot h^{-1}$)		Quantum efficiency (QE)	
				CO	CH_4	CO (%)	CH_4 (%)
Sample **1**	Short nanorod	2.39	37.8	3.11	0.58	0.36	0.065
Sample **2**	Polyhedron	2.63	10.9	1.18	0.31	0.14	0.035
Sample **3**	Nanocube	2.54	25.4	2.18	0.26	0.25	0.029

$CO_2 + 8\ e^- + 8H^+ \rightarrow CH_4 + 2H_2O$ ($E^o_{red} = -0.24$ V vs. NHE, pH = 7.00)

Meanwhile, the photogenerated holes in the valence band oxidize the H_2O to generate hydrogen ions through the following reaction [1–3]:

$H_2O \rightarrow 1/2O_2 + 2H^+ + 2\ e^-$ ($E^\circ_{red} = 0.82$ V vs. NHE, pH = 7.00)

Thus, the reduction capability of photogenerated electrons directly influences the reduction products. For instance, CO is produced with a just two electron reduction reaction, while the formation of CH_4 requires eight electrons. Therefore, it can be concluded that formations of main products like CO, CH_4, etc., are intensely related to the reduction ability of electrons. Several facts may explain the preferable production of CO including the multielectron transfer pathway, potential decomposition of CH_4 to CO, and effective formation of required number of electrons and protons.

The larger surface area provides relatively higher adsorption and more active sites, which could accelerate CO_2 adsorption and enhance its photocatalytic activity. The higher the surface areas that the catalyst possesses, the more reactants (e.g., active sites and$\cdot CO_2^-$ radical) are efficiently adsorbed on the surface leading to high photocatalytic efficiency [40,41]. The specific surface areas of sample **1**–sample **3** were measured by nitrogen adsorption–desorption approach (Fig. 5), and were estimated to be 37.8 $m^2 \cdot g^{-1}$, 10.9 $m^2 \cdot g^{-1}$ and 25.4 $m^2 \cdot g^{-1}$, respectively. Clearly, sample **1** exhibits the highest surface area (37.8 $m^2 \cdot g^{-1}$), while the smallest one is obtained in polyhedron morphology of sample **2**. As predicted, with larger surface area, the sample **1** exhibits better CO_2 photoreduction activity over the rest of the samples under same reaction conditions. The CO_2 reduction product generation efficiency of the CO and CH_4 over samples are quite consistence with expected results and with in order of sample **1** > sample **3** > sample **2** for CO production, and sample **1** > sample **2** > sample **3** for CH_4 formation, respectively. Thus, the relatively larger BET surface area of sample **1** is contributing its improved efficiency. Moreover,

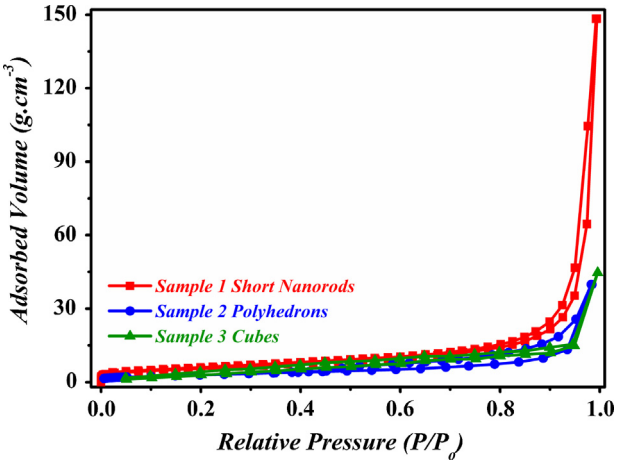

Fig. 5. Nitrogen adsorption–desorption isotherms of sample **1**–**3**.

the enhanced photoreduction efficiency of sample **1** can be ascribed to its unique short nanorods morphology due to orientated crystal growth, which led to fast charge transfer and facilitate carrier separation in orientated direction.

The sample **2** displays the smallest surface area (10.9 $m^2 \cdot g^{-1}$), though still gives certain photoreduction efficiencies. Observed photocatalytic effectiveness in sample **2** can be ascribed to its well crystalline surface character. As the case of uniform cube in sample **3**, the surface area and high degree of crystallinity co-contribute its photocatalytic performance. It is found that sample **1** exhibits the highest surface area (37.8 $m^2 \cdot g^{-1}$) than other samples, though gives 0.0823 $\mu mol \cdot g^{-1} \cdot h^{-1} \cdot m^{-2}$ and 0.015 $\mu mol \cdot g^{-1} \cdot h^{-1} \cdot m^{-2}$ generation for CO and CH_4, respectively, when obtained efficiencies are normalized to its surface area. Interestingly, the sample **3** has second highest surface area (25.4 $m^2 \cdot g^{-1}$), however shows the lowest efficiency for CO evolution (0.010 $\mu mol \cdot g^{-1} \cdot h^{-1} \cdot m^{-2}$) when the results normalized to its surface specific. On the basis of above results and discussions, it can be concluded that besides surface area, the other surface properties may be crucial for CO_2 reduction.

To further understand the differences in the photocatalytic responses across the various morphological samples, the optical properties and energy band configurations are discussed in the context of their relative light absorptions and redox capabilities of excited–state electrons and holes. Light absorption properties of the $CeTiO_4$ samples were analyzed (Fig. 6a), and the Kubelka–Munk method based on the diffuse reflectance spectra was employed to determine the band gaps [42]. As depicted in the inset of Fig. 6b and summed up results in Table 2, the corresponding band gaps of sample **1**–sample **3** are at 2.39 eV, 2.63 eV and 2.54 eV, respectively. These results show that all samples exhibit the same absorption extending into the visible light region, suggesting that observed photocatalysts response is significantly in the visible light region. Different from previously reported Ce-Ti phases of reddish-brown $Ce_2Ti_2O_7$, Ce_2TiO_5 and chestnut $Ce_4Ti_9O_{24}$, obtained samples display a yellow color (Inset in Fig. 6a) [25,43,44]. This further demonstrates that the as-obtained samples produce the Ce^{4+} species rather than Ce^{3+} since only two $CeTiO_4$ and $CeTi_2O_6$ phases show a similar yellow color [24,26]. It is particularly worth mentioning that after the Ce_2O_3 incorporation, the light absorption ranges of samples significantly increased from 3.21 eV to 2.54 eV compared with parent oxide TiO_2 (3.21 eV). Such significant changes in the light absorption edges of desired nanostructured samples demonstrate the crucial role of Ce_2O_3 in TiO_2 systems, suggesting its successful incorporation into the lattice of TiO_2, not simply dispersion on its surface. As it can be seen from Fig. 6a, the light absorptions show sharp decrease and tail up to about 550 nm, indicating the lattice defects (oxygen vacancies, V_O) in samples.

On the other hand, the strong and broad absorptions at around 300 nm–500 nm represent different excitations. The electron excitations from O $2p^6$ to Ti $3d^0$ come from TiO_6 octahedrons at 366 nm, which are strong in all samples [31]. Compared with the previously reported Ce—Ti compounds, as-obtained samples show stronger visible light absorption within the range of 449–518 nm, which comes from the electron transfer between Ce^{3+}/Ce^{4+} and defects [25,45,46]. It also indicates more active site and photon excitation occurs in this structure because of Ce 4f states are predominant at the valence band, while the

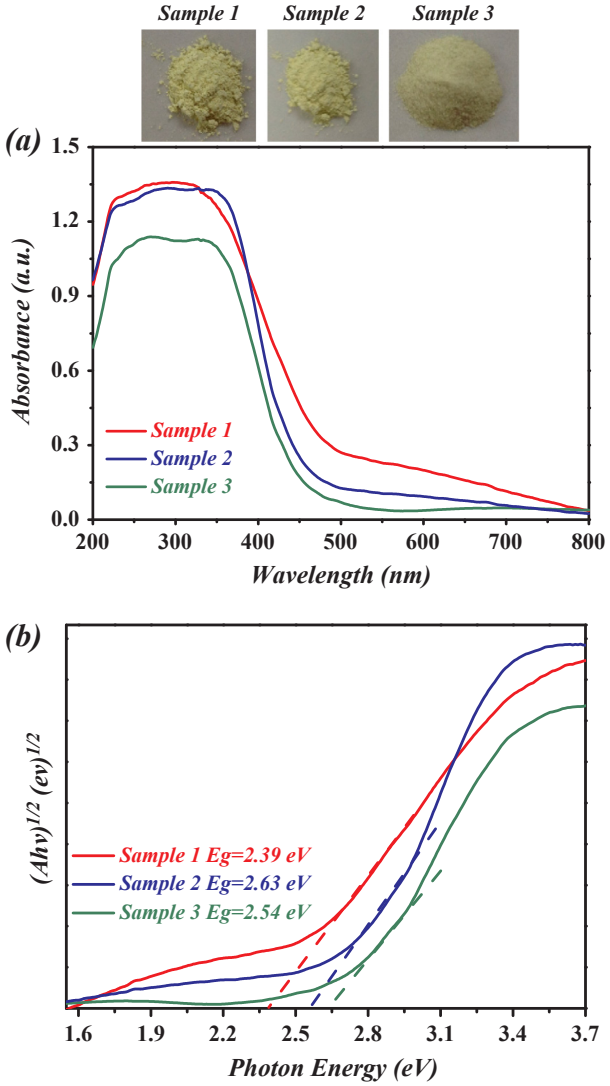

Fig. 6. (a) Room-temperature UV–vis absorption spectra of as-prepared samples; (b) Corresponding optical adsorption edges of sample **1**–sample **3**.

conduction band is mainly composed of Ti 3d orbital [47]. The presence of Ce^{4+} in the structure can generate charge transfer since the photogenerated electron is transferred to the empty 3d orbitals of Ti^{4+} ion, which is the source of the yellow colour in the samples. Additionally, the cerium titanate's strong visible light absorptions may originate from defects, such as oxygen vacancies.

The electron paramagnetic resonance (EPR) measurements were carried out to the further clarification the existence of defects in the structure. As exhibited in Fig. 7, four characteristic EPR signals with the g value of about 2.032, 2.003, 1.9782 and 1.9654 are observed in sample **1**–sample **3**, indicating various defects and species. The detected representative EPR signal corresponding to the $g = 2.003$ is caused by electrons trapped on surface oxygen vacancies with different widths [32]. In cerium titanates, the defects associated with oxygen, for instance, oxygen deficiency, oxygen at interstitial vacancy and even the holes on lattice oxygen are considered as a color centre, which is quite consistence with sample's light absorptions and observed colors from primrose to yellow (in the inset in Fig. 6a). However, relatively weaker representative EPR signal with this g value ($g = 2.003$) is observed in sample **1**, demonstrating the presence of trace amounts of oxygen deficiencies. Besides, the observed EPR signals appear at around the g value of 1.9654 are captured in sample **1**–sample **3**, which could be ascribed to characteristic signals of Ti^{3+}, though with relatively lower

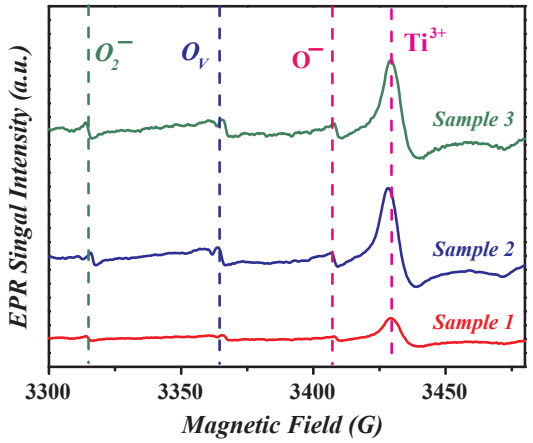

Fig. 7. Low temperature EPR spectra of sample **1**–sample **3**.

intensities for sample **1** among the studied samples. The existence of surface Ti^{3+} is expected enhance surface adsorbed atmospheric O_2, which results in superoxide radicals as a result of generated electrons trapped on surface V_O sites [48,49]. This corresponds to the anisotropic EPR signal appearing at around a g value of 2.032. These superoxide radical anions are observed in all studied samples, though sample **1** exhibits a relatively weaker signal, demonstrating that the trace amounts of superoxide radicals within. Besides the EPR signals with lower intensities at around $g = 1.9782$ are detected in sample **1**–sample **3**, which might be attributed to the O^-. These captured defects of Ce^{3+}, Ti^{3+} and observed trace amounts of O^- would enlarge light absorption ranges, promote carrier separations and in turn, enhance the photocatalytic efficiency. On the basis of observed not much defect differences in the studied $CeTiO_4$ samples, it can be concluded that the surface defects are confirmed as minor significant factor contributing high performance effectiveness towards CO_2 reduction.

Importantly, captured defects and trace amounts of O^- species, electron transformation between metals of Ce^{3+}/Ce^{4+} and Ti^{3+}/Ti^{4+}, and the redox role of Ce element in the structure are promoting carrier separations as revealed by photocurrent response tests (Fig. 8). Results showed that as-obtained samples display assorted photocurrent responses when the light is successively switched on and off. The higher photocurrent intensity implying more effective carrier separation in short nanorods, which could facilitate carrier mobility towards specific orientation. Interestingly, with nanocube shapes, sample **3** gives second higher photocurrent intensity, while sample **2** exhibits almost same carrier separation. It can be assumed that unique morphologies enhance the electron mobility by reducing carrier recombination, thus subsequently the effective charge carrier separations.

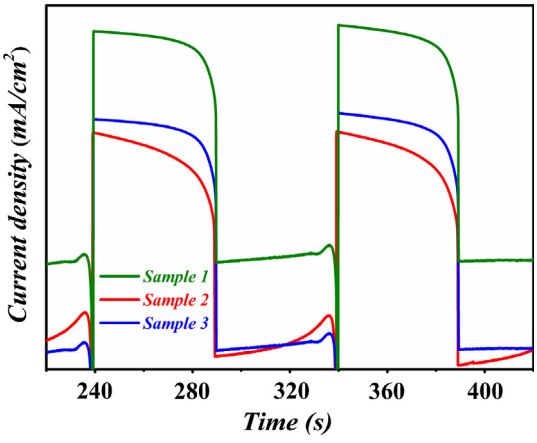

Fig. 8. Photocurrent responses of sample **1**–sample **3**.

To answer why the CO is preferably formed over as-obtained samples and to determine whether the band gaps can affect formation reduction products, the thermodynamics and band edge positions are taken into account. The bottom of the conduction band (CB) and the top of the valence band (VB) can be estimated empirically according to relationship between band edge energies and electronegativity, which can be expressed with the following equations [50]:

$$E_{CB} = \chi - E_C - 0.5E_g \quad (1)$$

$$E_{VB} = E_g + E_{CB} \quad (2)$$

where E_{CB} is the conduction band potential, χ is absolute electronegativity of the semiconductor, calculated as the geometric mean of absolute electronegativity of consisting elements $\chi = (\chi_A{}^a \chi_B{}^b \chi_C{}^c)^{1/(a+b+c)}$; E_C is a scale factor, taken as -4.5 eV; E_g is the band gap of semiconductor.

TiO_2 is a wide band gap semiconductor (3.21 eV) which absorbs only the ultraviolet fraction of the solar spectrum. According to these empirical equations, the conduction band minimum (CBM) of TiO_2 is more favourable for CH_4 formation than CO since its CBM is $E^o_{CB} = -0.29$ eV, higher than CH_4 generation potentials of $E^o_{red}(CO_2/CH_4 = -0.24$ V vs. NHE), though below production redox potentials of CO ($E^o_{red}CO_2/CO = -0.53$ V vs. NHE). This result implying that TiO_2 is inclining to generates CH_4 rather than CO during the photocatalytic reaction, thermodynamically. Alternatively, narrow band gap semiconductor Ce_2O_3 (2.40 eV) has a relatively negative CBM of $E^o_{CB} = -2.18$ eV, favourable for both CH_4 and CO production. However, its valence band minimum (VBM) is 0.216 eV, are not favourable for H^+ formation as it is more negative than $H_2O/2H^+$ ($E^\circ_{redox} = 0.82$ V vs. NHE), which makes it only suitable for the reduction reaction and not an efficient photocatalyst. The band gaps of as-obtained $CeTiO_4$ samples are within the visible light region and the CBM (E^o_{CB}) of the synthesized samples are predicted to be -0.879 eV (sample **1**), -0.999 eV (sample **2**) and -0.954 eV (sample **3**), all of which are more negative than required potential for CO and CH_4 production ($E^o_{red}(CO_2/CH_4 = -0.24$ V vs. NHE) and $E^o_{red}(CO_2/CO = -0.53$ V vs. NHE). Similarly, the VBM (E^o_{VB}) for sample **1**–sample **3** are estimated to be 1.511 eV, 1.631 eV and 1.586 eV, which are more positive than the potential of $H_2O/2H^+$ ($E^\circ_{redox} = 0.82$ V vs. NHE). Thus, we assume herein that, the main factor for preferable CO production over CH_4 is due to the more reasonable thermodynamics. Importantly, the simple incorporation of visible light active semiconductor (Ce_2O_3) into the UV sensitive metal oxide (TiO_2) offers an opportunity to improve light absorptions and efficient visible light driven photocatalysis in samples. Moreover, this simple corporation results in unique electrical properties as the result of a decreased band gap and suitable energy levels with contributions from both of the parent compounds. The higher conduction band minimum is favourable to produce more electrons, which will migrate to the surface of samples and thus induce the photoreduction reaction [1–3]. Herein, the preference for CO production over CH_4 is likely due to the fact that CH_4 requires double the number of electrons and is therefore kinetically limited. The band edge positions of TiO_2, Ce_2O_3 and leading performing sample **1** are shown in Fig. 9 relative to the redox potentials for the necessary reactions.

On the bases of the above-mentioned results and thermodynamics of precursors TiO_2, Ce_2O_3 and as-obtained $CeTiO_4$ samples, it is reasonable to conclude that both parent semiconductors are favourable for the selective formation of CO because of the suitable thermodynamics and appropriate band edge positions. The cation doped (i., Ce doped) TiO_2 displayed high efficiency for CO_2 reduction under visible light irradiation because inserting cations could create new impurity energy levels to enhanced the charge transfer. However, the concentration of Ce significantly influenced the photoreduction activity and is hard to control. The excessive amounts of Ce would inhibit the reaction as it becomes new carrier recombination centre [51]. It should be pointed out that, the pure phases of the assorted morphological $CeTiO_4$ samples not only gave higher efficiency for CO_2 reduction, but the effective charge separation was not related to doping and was not influenced by other factors, such as amounts of doped elements. Besides, the ceria-enriched compounds such as studied $CeTiO_4$ catalysts, can improve redox properties due to the Ce^{4+}/Ce^{3+} coupling, similar or even easier than that of Ti-based materials [3]. More importantly, in our experiment, we did not introduce any noble metals or co-catalysts. There is a room for the further investigations to design and explore even more promising catalyst for visible light driven CO_2 photoreduction with doping or apply cocatalysts. Therefore, highly efficient photoreduction activity of samples was achieved merely by incorporating visible light sensitive semiconductor (Ce_2O_3) into UV-active TiO_2 without doping.

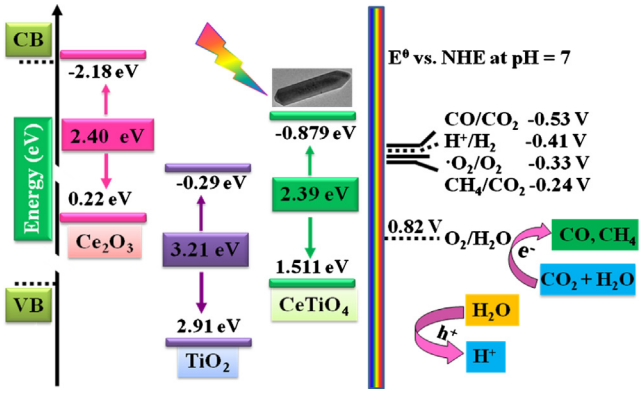

Fig. 9. Band-edge positions of semiconductor photocatalysts Ce_2O_3, TiO_2, $CeTiO_4$ and the relative to the energy levels of various redox couples.

4. Conclusions

In summary, Ti-based photocatalyst $CeTiO_4$ was successfully synthesized via a facile, one-step molten salt method. The nanorods, polyhedron and cube shaped morphologies of $CeTiO_4$ were obtained by employing different salt systems. Diverse microstructure (morphology), strong light absorption and color formation are well explained. Photocatalytic activities of $CeTiO_4$ samples were evaluated by photoreduction of CO_2 into valuable fuels. The forging four merits are highlighted in this contribution:

(i) Simple incorporation of visible light sensitive semiconductor Ce_2O_3 into UV active metal oxide TiO_2 without doping, which resulted in the yellowish pure phase of $CeTiO_4$ band gap being successfully adjusted.
(ii) Tailoring the morphology was achieved merely by changing the salt compositions during the molten salt synthesis process with a relatively low calcination temperature. The synthetic method represents a significant improvement over traditional methods to prepare complex oxides, which require very high calcination temperatures and long durations. The as-obtained samples exhibit nanoscale morphology, which is reported for the first time.
(iii) On the bases of light absorption, defect analyses and energy band configurations of diverse morphological $CeTiO_4$, the intrinsic correlation between the morphology, surface property and enhanced photoreduction performance was revealed. The best photoconversion of CO_2 was observed for short nanorod morphology of $CeTiO_4$ with the quantum efficiencies of about 0.36% and 0.065% for CO and CH_4 generation, respectively. The prepared samples exhibit higher conduction band minimum, which is favorable to produce more electrons, and will in turn leading to reduction.
(iv) More significantly, all samples demonstrated selective CO formation rather than CH_4. Higher efficiency of distinct morphological $CeTiO_4$ and selective CO generation is not only attributed to their

suitable thermodynamics, assorted morphologies and surface properties, but related to the efficient electron-hole production and suitable band edge position as a result of strong visible light absorptions, which are directly benefited from the successful incorporation of visible light active catalysts into a UV responsive semiconductor. The cooperation of semiconductor catalysts without doping and their photoreduction activity such as $CeTiO_4$ for CO selective formation, may pave the way for design and fabrication of new photocatalytic materials towards highly efficient conversion of solar energy for the greenhouse gases and find good application in the fields of environmental science.

Acknowledgements

The authors are grateful to the financial support of the NSFC (Grant No. 21473248), the CAS/SAFEA International Partnership Program for Creative Research Teams.

References

[1] J.L. White, M.F. Baruch, J.E. Pander III, Y. Hu, I.C. Fortmeyer, J.E. Park, T. Zhang, K. Liao, J. Gu, Y. Yan, T.W. Shaw, E. Abelev, A.B. Bocarsly, Light-driven heterogeneous reduction of carbon dioxide: photocatalysts and photoelectrodes, Chem. Rev. 115 (2015) 12888–12935.
[2] R. Shi, G.I.N. Waterhouse, T.R. Zhang, Recent progress in photocatalytic CO_2 reduction over perovskite oxides, Sol RRL 1 (2017) 1700126.
[3] W.G. Tu, Y. Zhou, Z.G. Zou, Photocatalytic conversion of CO_2 into renewable hydrocarbon fuels: state-of-the-art accomplishment, challenges, and prospects, Adv. Mater. 26 (2014) 4607–4626.
[4] M. Halmann, Photoelectrochemical reduction of aqueous carbon dioxide on p-type Gallium Phosphide in liquid junction solar cells, Nature 275 (1978) 115–116.
[5] T. Inoue, A. Fujishima, S. Konishi, K. Honda, Photoelectrocatalytic reduction of carbon dioxide in aqueous suspensions of semiconductor powders, Nature 277 (1979) 637–638.
[6] Y. Ma, X.L. Wang, Y.X. Jia, X.B. Chen, H.X. Han, C. Li, Titanium dioxide-based nanomaterials for photocatalytic fuel generations, Chem. Rev. 114 (2014) 9987–10043.
[7] Y.K. Sohna, W.X. Huang, F. Taghipour, Recent progress and perspectives in the photocatalytic CO_2 reduction of Ti-oxide-based nanomaterials, Appl. Sur. Sci. 396 (2017) 1696–1711.
[8] J.X. Low, B. Cheng, J.G. Yu, Surface modification and enhanced photocatalytic CO_2 reduction performance of TiO_2: a review, Appl. Sur. Sci. 392 (2017) 658–686.
[9] X.F. Zhu, B. Cheng, J.G. Yu, W.K. Ho, Halogen poisoning effect of Pt-TiO_2 for formaldehyde catalytic oxidation performance at room-temperature, Appl. Sur. Sci. 364 (2016) 808–814.
[10] Q. Liu, Y. Zhou, J.H. Kou, X.Y. Chen, Z.P. Tian, J. Gao, S.C. Yan, Z.G. Zou, High-yield synthesis of ultralong and ultrathin Zn_2GeO_4 nanoribbons toward improved photocatalytic reduction of CO_2 into renewable hydrocarbon fuel, J. Am. Chem. Soc. 132 (2010) 14385–14387.
[11] W.G. Tu, Y. Zhou, S.C. Feng, Q.F. Xu, P. Li, X.Y. Wang, M. Xiao, Z.G. Zou, Hollow spheres consisting of $Ti_{0.91}O_2$/CdS nanohybrids for CO_2 photofixation, Chem. Commun. 51 (2015) 13354–13357.
[12] S.C. Yan, S.X. Ouyang, J. Gao, M. Yang, J.Y. Feng, X.X. Fan, L.J. Wan, Z.S. Li, J.H. Ye, Y. Zhou, Z.G. Zou, A Room-temperature reactive-template route to mesoporous $ZnGa_2O_4$ with improved photocatalytic activity in reduction of CO_2, Angew. Chem. Int. Ed. 49 (2010) 6400–6404.
[13] L. Shi, T. Wang, H.B. Zhang, K. Chang, J.H. Ye, Electrostatic self-assembly of nanosized carbon nitride nanosheet onto a Zirconium metal-organic framework for enhanced photocatalytic CO_2 reduction, Adv. Funct. Mater. 25 (2015) 5360–5367.
[14] W.N. Wang, W.J. An, B. Ramalingam, S. Mukherjee, D.M. Niedzwiedzki, S. Gangopadhyay, P. Biswas, Size and structure matter: enhanced CO_2 photoreduction efficiency by size-resolved ultrafine Pt nanoparticles on TiO_2 single crystals, J. Am. Chem. Soc. 134 (2012) 11276–11281.
[15] A. Nikokavoura, C. Trapalis, Alternative photocatalysts to TiO_2 for the photocatalytic reduction of CO_2, Appl. Sur. Sci. 391 (2017) 149–174.
[16] H.L. Zhao, J.T. Chen, G.Y. Rao, W. Deng, Y. Li, Enhancing photocatalytic CO_2 reduction by coating an ultrathin Al_2O_3 layer on oxygen deficient TiO_2 nanorods through atomic layer deposition, Appl. Sur. Sci. 404 (2017) 49–56.
[17] M. Reli, M. Kobielusz, L. Matějová, S. Daniš, W. Macyk, L. Obalová, P. Strowski, A. Rokicińsk, K. Kočí, TiO_2 processed by pressurized hot solvents as a novel photocatalyst for photocatalytic reduction of carbon dioxide, Appl. Sur. Sci. 391 (2017) 282–287.
[18] G.S. Foo, G.X. Hu, Z.D. Hood, M.J. Li, D.E. Jiang, Z.L. Wu, Kinetics and mechanism of methanol conversion over anatase titania nanoshapes, ACS Catal. 8 (2017) 5345–5356.
[19] L.J. Liu, Y.Q. Jiang, H.L. Zhao, J.T. Chen, J.L. Cheng, K.S. Yang, Y. Li, Engineering coexposed 001 and 101 facets in oxygen-deficient TiO_2 nanocrystals for enhanced CO_2 photoreduction under visible light, ACS Catal. 6 (2016) 1097–1108.
[20] J.G. Yu, J.X. Low, W. Xiao, P. Zhou, M. Jaroniec, Enhanced photocatalytic CO_2 reduction activity of anatase TiO_2 by coexposed 001 and 101 facets, J. Am. Chem. Soc. 136 (2014) 8839–8842.
[21] T. Montini, M. Melchionna, M. Monai, P. Fornasiero, Fundamentals and catalytic applications of CeO_2-based materials, Chem. Rev. 116 (2016) 5987–6041.
[22] Y. Xu, M.A.A. Schoonen, The absolute energy positions of conduction and valence bands of selected semiconducting minerals, Am. Miner. 85 (2000) 543–556.
[23] K. Yoshii, Structural and magnetic studies of the lanthanide deficient perovskite $Ce_{2/3}TiO_3$, J. Alloy. Compd. 605 (2000) 72–75.
[24] S. Otsuka-Yao-Matsuo, T. Omata, M. Yoshimura, Photocatalytic behavior of cerium titanates, $CeTiO_4$ and $CeTi_2O_6$ and their composite powders with $SrTiO_3$, J. Alloy. Compd. 376 (2004) 262–267.
[25] W.S. Kim, J.K. Yang, C.K. Lee, H.S. Lee, H.H. Park, Synthesis and characterization of ferroelectric properties of $Ce_2Ti_2O_7$ thin films with Ce^{3+} by chemical solution deposition, Thin Solid Films 517 (2008) 506–509.
[26] L.T. Huynh, S.B. Eger, J.D.S. Walker, J.R. Hayes, M.W. Gaultois, A.P. Grosvenor, How temperature influences the stoichiometry of $CeTi_2O_6$, Solid State Sci. 14 (2012) 761–767.
[27] Y.J. Ma, Z.M. Wang, X.F. Xu, J.Y. Wang, Review on porous nanomaterials for adsorption and photocatalytic conversion of CO_2, Chinese J. Catal. 38 (2017) 1956–1969.
[28] T.M. Di, J.F. Zhang, B. Cheng, J.G. Yu, J.S. Xu, Hierarchically nanostructured porous TiO_2 (B) with superior photocatalytic CO_2 reduction activity, Sci. China. Chem. 61 (2018) 344–350.
[29] R. Hailili, C.Y. Wang, E. Lichtfouse, Perovskite nanostructures assembled in molten salt based on halogen anions KX (X = F, Cl and Br): regulated morphology and defect-mediated photocatalytic activity, Appl. Catal. B 232 (2018) 531–543.
[30] R. Hailili, Z.-Q. Wang, Y.X. Li, Y.H. Wang, K.S. Virender, X.-Q. Gong, C.Y. Wang, Oxygen vacancies induced visible-light photocatalytic activities of $CaCu_3Ti_4O_{12}$ with controllable morphologies for antibiotic degradation, Appl. Catal. B 221 (2018) 422–432.
[31] R. Hailili, G.H. Dong, S. Jin, C.Y. Wang, T. Xu, Layered perovskite $Pb_2Bi_4Ti_5O_{18}$ for excellent visible light-driven photocatalytic NO removal, Ind. Eng. Chem. Res. 56 (2017) 2908–2916.
[32] H. Yaghoubi, Z. Li, Y. Chen, H.T. Ngo, V.R. Bhethanabotla, B. Joseph, S.Q. Ma, R. Schlaf, A. Takshi, Toward a visible light-driven photocatalyst: the effect of mid gap-states-induced energy gap of undoped TiO_2 nanoparticles, ACS Catal. 5 (2015) 327–335.
[33] V. Jeyalakshmi, R. Mahalakshmy, K. Ramesh, P.V.C. Rao, et al., Visible light driven reduction of carbon dioxide with water on modified $Sr_3Ti_2O_7$ catalysts, RSC Adv. 5 (2015) 5958–5966.
[34] Y.X. Li, G. Chen, Q. Wang, X. Wang, A.K. Zhou, et al., Hierarchical ZnS-In_2S_3-CuS nanospheres with nanoporous structure: facile synthesis, growth mechanism, and excellent photocatalytic activity, Adv. Funct. Mater. 20 (2010) 3390–3398.
[35] M.F. Luo, J. Chen, L.S. Chen, J.Q. Lu, Z.C. Feng, C. Li, Structure and redox properties of $Ce_xTi_{1-x}O_2$ solid solution, Chem. Mater. 13 (2001) 197–202.
[36] P. Li, Y. Zhou, Z.Y. Zhao, Q.F. Xu, X.Y. Wang, M. Xiao, Z.G. Zou, Hexahedron prism-anchored octahedronal CeO_2: crystal facet-based homojunction promoting efficient solar fuel synthesis, J. Am. Chem. Soc. 137 (2015) 9547–9550.
[37] S.H. Zhang, S. Muratsugu, N. Ishiguro, S.-I. Ohkoshi, M. Tada, Perovskite $NaCeTi_2O_6$ supported Ni catalysts for CH_4 steam reforming, ChemCatChem. 4 (2012) 1783–1790.
[38] J.Q. Jiao, Y.C. Wei, Z. Zhao, J. Liu, J.M. Li, A.J. Duan, G.Y. Jiang, Photocatalysts of 3D ordered macroporous TiO_2-supported CeO_2 nanolayers: design, preparation, and their catalytic performances for the reduction of CO_2 with H_2O under simulated solar irradiation, Ind. Eng. Chem. Res. 53 (2014) 17345–17354.
[39] B.C. Yu, Y. Zhou, P. Li, W.G. Tu, P. Li, L.Q. Tang, J.H. Ye, Z.G. Zou, Photocatalytic reduction of CO_2 over Ag/TiO_2 nanocomposites prepared with a simple and rapid silver mirror method, Nanoscale 8 (2016) 11870–11874.
[40] J.J. Wang, G.N. Li, Z.L. Li, C.Z. Tang, Z.C. Feng, H.Y. An, H.L. Liu, T.F. Liu, C. Li, A Highly selective and stable ZnO-ZrO_2 solid solution catalyst for CO_2 hydrogenation to methanol, Sci. Adv. 3 (2017) e1701290.
[41] F. Wang, S. He, H. Chen, B. Wang, L.R. Zheng, M. Wei, D.G. Evans, X. Duan, Active site dependent reaction mechanism over Ru/CeO_2 catalyst toward CO_2 methanation, J. Am. Chem. Soc. 138 (2016) 6298–6305.
[42] P. Kubelka, F. Munk, An article on optics of paint layers, Z. Tech. Phys. 12 (1931) 593–601.
[43] A. Preuss, R. Gruehn, Preparation and structure of cerium titanates Ce_2TiO_5, Ce_2TiO_7, and $Ce_4Ti_9O_{24}$, J. Solid State Chem. 110 (1994) 363–369.
[44] M. Martos, B. Julián-López, J.V. Folgado, E. Cardoncillo, P. Escribano, Sol-gel synthesis of tunable cerium titanate materials, Eur. J. Inorg. Chem. 2008 (2008) 3163–3171.
[45] S.M. Fang, Y.J. Xin, L. Ge, C.C. Han, P. Qiu, L.N. Wu, Facile synthesis of CeO_2 hollow structures with controllable morphology by template-engaged etching of Cu_2O and their visible light photocatalytic performance, Appl. Catal. B 179 (2015) 458–467.
[46] S. Agarwal, X. Zhu, E.J.M. Hensen, B.L. Mojet, L. Lefferts, Surface-dependence of defect chemistry of nanostructured ceria, J. Phys. Chem. C 119 (2015) 12423–12433.
[47] C.W. Sun, H. Li, L.Q. Chen, Nanostructured ceria-based materials: synthesis, properties, and applications, Energy Environ. Sci. 5 (2012) 8475–8505.
[48] S.G. Kumar, K.S.R.K. Rao, Comparison of modification strategies towards enhanced charge carrier separation and photocatalytic degradation activity of metal oxide semiconductors (TiO_2, WO_3 and ZnO), Appl. Sur. Sci. 391 (2017) 124–148.
[49] X.M. Yu, B. Kim, Y.K. Kim, Highly enhanced photoactivity of anatase TiO_2 nanocrystals by controlled hydrogenation-induced surface defects, ACS Catal. 3 (2013) 2479–2486.
[50] R.G. Pearson, Absolute electronegativity and hardness: application to inorganic chemistry, Inorg. Chem. 27 (1988) 734–740.
[51] X.F. Yang, S. Kattel, et al., Low pressure CO_2 hydrogenation to methanol over gold nanoparticles activated on a CeO_x/TiO_2 interface, J. Am. Chem. Soc. 137 (2015) 10104–10107.